Toward an Algorithm for Estimating Latent Heat Release in Warm Rain Systems

ETHAN L. NELSON AND TRISTAN S. L'ECUYER

Department of Atmospheric and Oceanic Sciences, University of Wisconsin–Madison, Madison, Wisconsin

STEPHEN M. SALEEBY, WESLEY BERG, STEPHEN R. HERBENER, AND SUSAN C. VAN DEN HEEVER

Colorado State University, Fort Collins, Colorado

(Manuscript received 8 October 2015, in final form 20 April 2016)

ABSTRACT

This paper outlines an approach for estimating latent heating, surface rainfall rate, and liquid water path in warm rain from downward-viewing W-band radar observations using a Bayesian Monte Carlo algorithm. The algorithm utilizes observed vertical and path-integrated characteristics of precipitating liquid clouds to identify the most appropriate hydrometeor and latent heating structures in a large database of profiles generated using a cloud-resolving model. These characteristics are selected by applying multiple performance metrics to synthetic retrievals. Analysis of the retrievals suggests that a combination of cloud-top, rain-top, and maximum reflectivity heights; vertically integrated reflectivity and attenuation; and a measure of near-surface intensity is sufficient to constrain bulk properties and the vertical structure of warm rain systems. When applied to observations at *CloudSat* resolution, biases in retrieved liquid water path and surface rainfall rate are small (less than 10%). The algorithm also captures the vertical structure of latent heating, although the magnitudes of integrated heating and cooling exhibit nearly compensating low biases. Random errors are larger owing to the limitations of single-frequency radar observations in constraining drop size distributions. Uncertainties in the altitudes of peak heating and cooling at the pixel scale are typically less than one vertical level, while uncertainties in vertically resolved estimates of heating and cooling rates are on the order of a factor of 2. The utility of the technique is illustrated through application to case studies from airborne radar data from the VAMOS Ocean–Cloud–Atmosphere–Land Study field campaign and satellite observations from *CloudSat*.

1. Introduction

The release of latent heat provides a mechanism for transferring energy from the surface to the upper atmosphere. Latent heating due to phase changes of water in cloud and precipitation formation and dissipation processes helps drive the atmospheric general circulation, and an accurate accounting of its three-dimensional distribution is necessary to correctly model the climate system (Simpson et al. 1988). Aubert (1957) determined that latent heat release affects vertical motion in the surrounding environment, with the height of maximum release corresponding to the level of maximum velocity perturbation. Near the same time, Riehl and Malkus (1958) found that tropical convection provides the necessary means of transferring energy from the lower atmosphere to the upper troposphere, which feeds the ascending branch of the Hadley circulation. This notion was based on the premise of ''hot towers,'' a term coined in the paper for what are considered today as convection turrets in the trimodal distribution of convection within tropical regions (Johnson et al. 1999).

While it is possible to infer net latent heat release in a domain from total precipitation accumulations, the impact of this heating depends on its vertical placement in the atmosphere. Using a linearized model, Hartmann

Corresponding author address: Ethan L. Nelson, Department of Atmospheric and Oceanic Sciences, University of Wisconsin–Madison, 1225 West Dayton Street, Madison, WI 53706.
E-mail: ethan.nelson@aos.wisc.edu

DOI: 10.1175/JTECH-D-15-0205.1

et al. (1984), for example, found that atmospheric circulations are sensitive to the vertical distribution of latent heating associated with widespread convection occurring in tropical regions. Full realistic vertical velocity and heating profiles in tropical regions were required to successfully recreate a circulation similar to that of the real atmosphere. Furthermore, the vertical distribution of latent heating differs substantially between regimes of deep convection and associated stratiform precipitation (Houze 1982). Convective regimes contain more total heating throughout the tropospheric extent of the cloud, while stratiform clouds usually contain a higher magnitude of evaporative cooling (McCumber et al. 1991; Mapes and Houze 1993; Tao et al. 1993). It has also been theorized that latent heating by condensation within the lower levels of the atmosphere from shallow convection plays an important role during the incipient stages of the Madden–Julian oscillation (MJO) (Jiang et al. 2011). Similarly, Sheffield et al. (2015) demonstrated that variations in the latent heat released by warm-phase processes impacted the transitions from shallow cumulus clouds to deep convection. Thus, a proper representation of warm rain, defined as that which forms exclusively from droplet collision and coalescence processes below the freezing level, and the latent heat released by it may be essential to correctly model the progression of the MJO and other climatic features (Jiang et al. 2011; Schumacher et al. 2004).

A number of methods have been explored for deriving latent heating estimates from both ground-based and satellite measurements, but observations of shallow precipitation are often underrepresented in conventional precipitation and latent heating datasets (Haynes and Stephens 2007; Ellis et al. 2009; Berg et al. 2010; Hagos et al. 2010; Jiang et al. 2009; Zhang et al. 2010; Lebsock and L'Ecuyer 2011). Efforts to quantitatively estimate latent heating from observations mostly stem from Reed and Recker (1971) and Yanai et al. (1973), who used heat and moisture budgets to calculate domain fluxes of diabatic heating from a modeling perspective and a distributed radiosonde network, respectively. Numerous studies have since applied similar methods to quantify diabatic heating in the atmosphere, usually in a targeted field campaign employing a variety of observation platforms. For example, the Tropical Ocean Global Atmosphere Coupled Ocean–Atmosphere Response Experiment provided datasets to calculate diabatic heating fluxes from a combination of radiosondes, radar, and other instruments (Johnson and Ciesielski 2000). Thompson et al. (1979) utilized diabatic heating estimates generated from a network of ship observations to study the growth of wave disturbances in the intertropical convergence zone during the GARP Atlantic Tropical Experiment. Schumacher et al. (2007, 2008) analyzed the idealized heating profiles of differing cloud types observed during multiple field campaigns using both radiosonde and radar observations. Latent heating estimates from airborne Doppler radar also have provided insights into the growth of a hurricane (Guimond et al. 2011; Guimond and Reisner 2012).

Calculations of regional heat budgets are prone to error due to 1) the required use of multiple instruments with different performance characteristics and calibrations and 2) the fragmented sampling of the area stemming from the spatial distribution of the observation sites (Mapes et al. 2003). Moreover, there is a need to understand latent heating on global scales that cannot be addressed using regional field campaigns. The launch of the Tropical Rainfall Measuring Mission (TRMM) paved the way for the development of satellite-based methods for inferring latent heat release throughout the tropics and subtropics from both active and passive sensors. A thorough review of many of the TRMM-based latent heating products can be found in Tao et al. (2016). The Goddard convective–stratiform heating product (Tao et al. 2010), for example, employs a lookup table generated mainly from tropical oceanic cloud-resolving model (CRM) simulations to retrieve latent heating using rain rate—a proxy for cloud depth—and cloud type. The hydrometeor heating product (Yang and Smith 1999), on the other hand, uses features of vertical velocity, rain rate, and the hydrometeor profile as input into a CRM to calculate latent heating. Yet another approach is the trained radiometer (TRAIN) algorithm (Olson et al. 1999), which utilizes a trained database of reflectivity and brightness temperature composites to estimate latent heating from passive microwave observations.

Of greatest similarity to the work presented here is the spectral latent heating (SLH) algorithm (Shige et al. 2004, 2007, 2008, 2009). SLH uses characteristics of a reflectivity profile, including the rain-top height and a cloud type classification, to retrieve latent heating from a model-generated lookup table. This methodology is effective because the vertical reflectivity structure correlates well with vertical variations in the drop size distribution although it is skewed to the largest drops in the size spectrum and hence does not accurately represent changes to the smaller drops. These variations represent the fingerprint of the liquid and ice processes occurring within the cloud, thus allowing the corresponding heating to be estimated with reasonable skill (Hagos et al. 2010). Isolated warm rain, however, poses a challenge for all TRMM precipitation radar (PR) algorithms due to the PR's high minimum

detectable reflectivity (+18 dBZ) and 4-km field of view (Kummerow et al. 1998; Berg et al. 2010).

It is reasonable to expect that a similar approach can be applied to any radar, including the *CloudSat* Cloud Profiling Radar (CPR), which has excellent sensitivity to lighter precipitation. *CloudSat* is an Earth observation satellite flying in the Afternoon constellation (A-Train) (Stephens et al. 2008; L'Ecuyer and Jiang 2010). A-Train satellites follow a sun-synchronous orbit that crosses the equator at around 1330 local time at an altitude of 690 km. The CPR is a W-band (94 GHz) nadir-viewing radar with a vertical resolution of 480 m (with backscatter oversampling increasing this to 240 m), a cross-track resolution of 1.4 km, and an instantaneous along-track resolution of about 1.75 km (Stephens et al. 2008; Tanelli et al. 2008). The minimum detectable reflectivity of the CPR is −30 dBZ, providing the sensitivity needed to observe lightly precipitating clouds that extend above the region obscured by ground clutter in the lowest 750 m of the atmosphere (Haynes et al. 2009).

Because of its high sensitivity, high spatial resolution, and collocation with other satellites in the A-Train, *CloudSat*'s CPR provides a unique perspective for inferring latent heating in shallow, lightly precipitating clouds. CPR observations are currently used in three precipitation algorithms that generate estimates of liquid and frozen precipitation over most of the globe (Haynes et al. 2009; Lebsock and L'Ecuyer 2011; Wood et al. 2014). These efforts have provided improved estimates of shallow rainfall in the tropics and overall precipitation in the extratropics, particularly in areas where a significant fraction of precipitation falls as snow (Rapp et al. 2013; Wood et al. 2014). The algorithms generally underestimate heavier precipitation due to the strong attenuation of the W band.

The main objective of this study is to test the hypothesis that downward-viewing W-band radar observations can constrain the magnitude of latent heating and other related cloud properties in lightly precipitating warm rain clouds. Though warm rain systems have been calculated to contribute up to 20% of global rainfall (Lin and Rossow 1997; Liu and Zipser 2009), the observation of these shallow systems is often underestimated (Berg et al. 2010). Successfully quantifying latent heat release in these warm rain clouds would help to complete the spectrum of latent heating estimates globally. We attempt this quantification through the design and implementation of a Bayesian Monte Carlo algorithm described in section 2. Results from testing the algorithm in a synthetic environment are presented in section 3, while examples of application to airborne data collected during a recent field campaign and a *CloudSat* granule are presented in section 4. The overall performance of the algorithm is summarized, with a discussion of forthcoming research and potential avenues of algorithm advancement, in section 5.

2. Algorithm design

a. *Bayesian framework*

Inferring latent heating from vertical profiles of reflectivity is not trivial because the reflectivities are only indirectly related to the associated microphysical processes through the resultant radar signatures. The observations must be connected to the *physical processes* through dynamical models. Bayesian Monte Carlo (BMC) methodologies are well suited for this inverse problem because they connect a generated a priori distribution of possible physical states to the observations in a probabilistic way. BMC retrievals have frequently been used in the remote sensing of cloud microphysical properties. Kummerow and Giglio (1994), for example, created a rainfall retrieval by employing a Bayesian estimate of the relationship between brightness temperatures and rainfall rate. Evans et al. (1995) directly applied the BMC method to retrieve vertical hydrometeor profiles from combined passive instrument channel observations.

One advantage of a BMC retrieval is that it provides the infrastructure to combine measurements of different types, potentially from different instruments. Further, this method provides not only a mean state but also the uncertainty based on the spread of the a posteriori distribution, which explicitly accounts for the relative accuracies associated with all observations through the assumed error covariance matrix. Larger variances will yield a more relaxed distribution, while smaller variances will narrow the solution set. Yet another advantage of the BMC approach is that no single assumption regarding physical characteristics of the state are required, such as a predefined cloud droplet number concentration. Instead, models or in situ observations that link such parameters to thermodynamic and dynamic conditions can be incorporated into the database simulations.

In general, a BMC retrieval takes an a priori distribution and updates it to an a posteriori distribution by reducing the possible solution set to include only those states that provide a close match to the observations. Mathematically, the vector of retrieved quantities is generated by comparing the vector of simulated observations $\mathbf{y}_s$ for all profiles in the algorithm database to the vector of observations $\mathbf{y}_o$ and assigning a probability p to each member i while accounting for the covariance $\mathbf{C}$ between the vector components:

$$p_i = \frac{\exp\left[-\frac{1}{2}(\mathbf{y}_o - \mathbf{y}_{s,i})^{\mathrm{T}}\mathbf{C}^{-1}(\mathbf{y}_o - \mathbf{y}_{s,i})\right]}{\sum_{j=1}^{N}\exp\left[-\frac{1}{2}(\mathbf{y}_o - \mathbf{y}_{s,j})^{\mathrm{T}}\mathbf{C}^{-1}(\mathbf{y}_o - \mathbf{y}_{s,j})\right]}, \quad (1)$$

where N is the number of database members. Following Bayes's theorem, the retrieved vector is the sum of the database profiles' quantities weighted by their associated probability:

$$\bar{x} = \sum_{i=1}^{N} \mathbf{y}_{\mathbf{s,i}}\mathbf{p}_{\mathbf{i}}. \quad (2)$$

The uncertainty in the retrieved quantity is the weighted standard deviation:

$$\sigma_x = \sqrt{\sum_{i=1}^{N}(\mathbf{y}_{\mathbf{s,i}} - \bar{x})^2\mathbf{p}_{\mathbf{i}}}. \quad (3)$$

For further discussion of this approach, see L'Ecuyer and Stephens (2002).

The key to producing quality retrievals with a BMC approach comes down to two factors: 1) generating a database of physically realistic realizations and 2) specifying an appropriate error covariance matrix that represents the relative accuracy of all component measurements and the correlations between them. In practice, these factors require several assumptions and choices regarding the source of information to include in the database and its completeness, and the current study is no exception. Since observational estimates of latent heat release in warm rain systems are very limited, a database of cloud-resolving model simulations is adopted here to illustrate the potential for retrieving latent heating in warm rain from W-band radar observations (described below), and an appropriate error covariance matrix is assembled as follows.

Variances σ form the diagonal element of the covariance matrix through assumed errors in the algorithm database and input. Off-diagonal elements of the covariance matrix represent correlations r between the errors in various parameters owing to effects like attenuation or sensitivities to forward model assumptions. The full covariances that fill in the off-diagonal elements of the covariance matrix are the product of the correlation and the assumed errors of each variable:

$$\mathbf{C} = \begin{bmatrix} \sigma_1\sigma_1 & r_{21}\sigma_2\sigma_1 & \cdots & r_{n1}\sigma_n\sigma_1 \\ r_{12}\sigma_1\sigma_2 & \sigma_2\sigma_2 & \cdots & r_{n2}\sigma_n\sigma_2 \\ \vdots & \vdots & \ddots & \vdots \\ r_{1n}\sigma_1\sigma_n & r_{2n}\sigma_2\sigma_n & \cdots & \sigma_n\sigma_n \end{bmatrix}. \quad (4)$$

b. Cloud-resolving model simulations

To supply an a priori database spanning the space of realistic warm rain states, the Regional Atmospheric Modeling System (RAMS) is employed. RAMS is a versatile, high-resolution, nonhydrostatic CRM with a bin-emulating two-moment bulk microphysics scheme (Cotton et al. 2003; Saleeby and Cotton 2004; Saleeby and van den Heever 2013). Size distributions of all hydrometeors in RAMS are defined by a modified gamma distribution, while mass–volume and terminal velocity relationships follow power laws. Mixing ratio and number concentration of cloud droplets, drizzle, and rain are used in this paper given the focus on warm rain processes.

Nine separate RAMS simulations are used to build the database employed here. Each simulation is initialized from composite soundings of the Atlantic Trade Wind Experiment (ATEX) over a domain in the tropical Atlantic Ocean bounded from 14.49° to 15.39°N and from 35.53° to 36.46°W with cyclical lateral boundary conditions (Saleeby et al. 2015). The model resolution is set to 250 m in the horizontal and 100 m in the vertical. Each horizontal dimension consists of 400 grid boxes, resulting in a 100 km by 100 km domain. A total of 40 equally spaced vertical layers are specified from the sea surface to a 4-km top with a 400-m-thick Rayleigh damping layer at the domain top. No large-scale forcing is imposed within the model in order to allow a variety of warm cloud types to form within the domain. Surface processes are parameterized using the "ocean" category from the Land Ecosystem–Atmosphere Feedback, version 3 (LEAF-3), surface model (Walko et al. 2000). The model is spun up for 12 h and then run for 24 additional hours with output variables computed every 5 min. The analysis presented here will utilize data from the entire 24-h period.

Each simulation has a distinct combination of sea surface temperature (SST) and maximum concentration of aerosols that can serve as cloud condensation nuclei (CCN) to capture a range of warm rain regimes that occur in distinct environments. SST is defined to be either 293, 298, or 303 K, while CCN concentrations of either 100, 400, or 800 per cubic centimeter (cc^{-1}) at the surface are chosen. Each model run is initialized with an idealized aerosol profile where the surface aerosol number concentration decreased linearly with height to the model top. Large regime differences result because of the varied environmental conditions between runs (Saleeby et al. 2015). At 293 K, the cloud cover is highly homogeneous in extent. For higher SSTs, much of the domain is cloud free as precipitation is confined to isolated convective cores. Some

modulation of precipitation intensity in response to change in aerosol concentration is present, most notably in the middle SST experiments, where lower aerosol environments are more homogeneous in precipitating cloud cover, while higher aerosol environments yield some convective cores.

c. Radar simulator

To translate RAMS hydrometeor species and atmospheric state output into a set of observables that might be seen by a radar surveying the real atmosphere, a radar simulator is applied to the model output. QuickBeam is a radar forward model that computes radar reflectivity and attenuation at a specified frequency given a model hydrometeor profile (Haynes et al. 2007). The unattenuated reflectivities are also calculated to estimate the path-integrated attenuation (PIA) resulting from hydrometeors. Microphysical distributions used in the radar simulator are chosen to match the RAMS two-moment microphysics scheme. For the purpose of retrieving latent heating from shallow clouds, W-band reflectivities consistent with CPR are simulated by QuickBeam. Scattering properties are defined using Mie theory, and no melting-layer model or complex scattering tables are necessary given the absence of ice-phase processes in these simulations.

d. Database properties

To populate the database with a set of realistic profiles, every eighth output time (or every 40 min) is sampled. This process yields a pool of profiles that are independent of each other while limiting the number included. Only profiles with a surface rainfall rate greater than or equal to 0.01 mm h^{-1} and at least one reflectivity bin exceeding 0 dBZ are processed, as the latter is the threshold used to define rain-certain profiles in the *CloudSat* 2C-PRECIP-COLUMN algorithm (Haynes et al. 2009). This procedure yields nearly 1.4 million valid realizations of warm rain from which the algorithm may search for a solution.

In addition to defining a measurement vector consisting of the full profile of reflectivity with PIA, seven different reflectivity profile parameters are defined in order to assess the potential for reducing computational cost by using a smaller observation vector in the algorithm. These parameters are listed in Table 1 and illustrated in Fig. 1. Starting from the top of the cloud, the height of the highest −30-dBZ echo, H_{-30}, is defined to represent the cloud-top level. Next, from the top down, the height of the 0-dBZ intersection H_0 is chosen to indicate the top of the rain column. The maximum reflectivity detected in the profile Z_M provides a measure of the largest drops in the profile, while the height of Z_M, H_M, provides information about the vertical distribution of condensate. Path-integrated reflectivity (PIR) serves as a measure of the integrated condensate drop spectrum within the cloud. The near-surface reflectivity Z_{1km} is defined as the reflectivity value closest to 1 km above ground and helps to discern the near-surface properties of the profile whenever a profile is not fully attenuated. The term Z_{1km} is also a bin height at which ground backscatter contamination is minimal on the CPR. Finally, the two-way PIA provides information about the integrated water mass within the cloud. Model values of LWP, surface rainfall rate, and the vertical profile of latent heating associated with each profile form the algorithm outputs.

TABLE 1. Description of the tested algorithm variables.

Variable	Description
H_{-30}	−30-dBZ height intersection starting from the top
H_0	0-dBZ height intersection starting from the top
PIR	Path-integrated reflectivity
PIA	Two-way path-integrated attenuation
Z_M	Profile maximum reflectivity value
H_M	Height of the profile maximum reflectivity value
Z_{1km}	Nearest to 1-km AGL reflectivity value

Assigned variances for the reflectivity parameters are consistent with the error characteristics of the *CloudSat* CPR (Tanelli et al. 2008). Reflectivity and PIR are assumed to have errors of 1 dBZ to match the signal-to-noise ratio of the CPR. Uncertainties due to forward model error owing to assumed drop size distributions are not included in this initial formulation, but they will be discussed later. Height errors are assumed to match approximately one vertical range bin of the radar (100 m for applications at native model resolution and 300 m when applied to *CloudSat* data). Estimates of PIA from the CPR are a function of the attenuated surface backscatter and the integrated extinction coefficient, having an estimated uncertainty of about 2 dB over the ocean (Haynes et al. 2009). Note that while a constant 2-dB error is assumed in the algorithm, the actual uncertainty in *CloudSat* PIA is a function of surface wind speed.

The correlations between variables are either 1) the computed linear Pearson correlation coefficients when integrated and height variables are used or 2) an exponential decay when full reflectivity profiles are used. Figure 2 displays two-dimensional histograms of several different characteristics of reflectivity profiles, as well as the associated inferred correlation matrices for all variable combinations and the full reflectivity profile. Distributions between the different parameters exhibit no clear linear relationship with the exception of PIR and

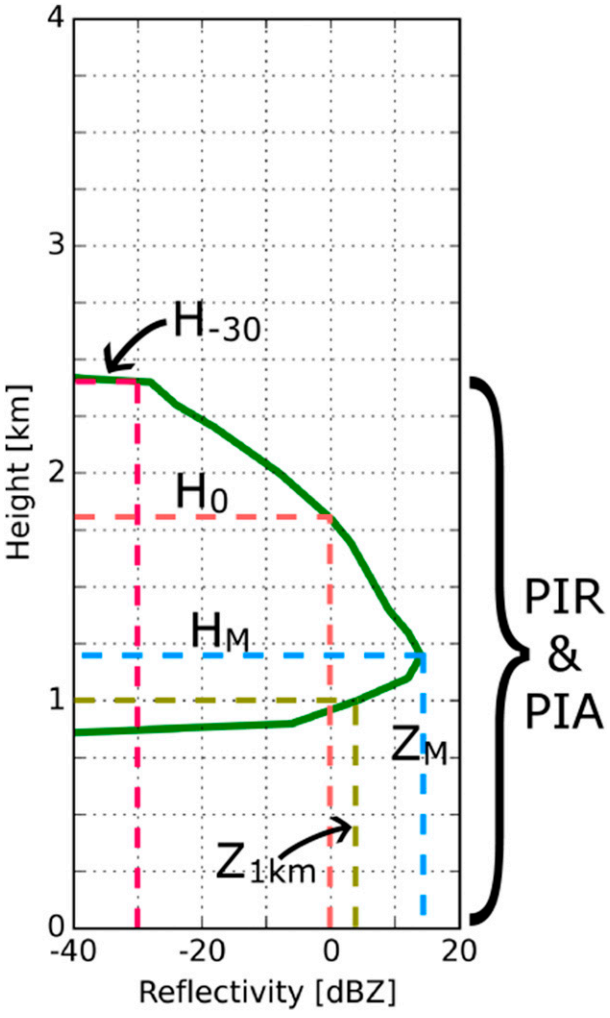

FIG. 1. Illustration of the tested algorithm parameters listed in Table 1 on a reflectivity profile (green): H_{-30} (red), H_0 (orange), H_M and Z_M (blue), $Z_{1\text{km}}$ (light green), PIR, and PIA.

Z_M. This is reflected in the fact that the correlation between PIR and Z_M (fourth row from the top, third column from the left) is the only quantity that approaches unity (0.975). Full reflectivity profile correlations r_i are assumed to decay exponentially as a function of height z_i above or below a given level z by a defined scale length L_s:

$$r_i = \begin{cases} \exp\left(-\dfrac{|z - z_i|}{L_s}\right), & \text{for} \quad |z - z_i| \le 2L_s \\ 0, & \text{for} \quad |z - z_i| > 2L_s \end{cases}. \quad (5)$$

This function is chosen to mathematically represent the correlations between errors in nearby reflectivity layers.

Because the aim of this study is to demonstrate application of the algorithm to *CloudSat*, two databases are created: one at the full model resolution that is used to test the algorithm and may be suitable for application to high-resolution airborne radar, and the other appropriate for application to *CloudSat* where model output is degraded to the resolution of the *CloudSat* footprint by averaging horizontally to construct a 1.5-km-diameter circular footprint and vertically to form 300-m-height bins.

e. Evaluation metrics

In addition to standard error statistics, other metrics can be used to assess the effectiveness of the algorithm. First, the maximum probability (hereafter referring to the maximum probability prior to normalization) is employed as a quality control check for the algorithm since this value is analogous to chi-squared through $p_i = \exp(-1/2\chi^2)$. Maximum probability and chi-squared exhibit opposite responses: very low maximum probabilities correspond to high values of chi-squared and describe a bad fit when the algorithm cannot find a close match to the observations anywhere in the database, while maximum probabilities near unity describe a good match in the database.

Second, entropy provides a useful measure of overall information content. Entropy is often associated with heat changes vis-à-vis thermodynamics, but it can also be applied to measure changes in information afforded by an observing system. The relative entropy, or Kullback–Leibler (KL) divergence, is defined[1] for discrete distributions as

$$D_{\text{KL}} = \sum_{i=1}^{N} p_i \log_2\left(\frac{p_i}{q_i}\right), \quad (6)$$

where p_i and q_i are the respective probabilities of a profile from different distributions (Kullback and Leibler 1951). In problems associated with non-Gaussian statistics, relative entropy is preferable over other information content metrics (e.g., the Shannon information content; Shannon 1948) as it provides a quantification of the distance between statistical populations, as opposed to simply measuring the change in width of two distributions (G. W. Petty 2016, personal communication). Relative entropy helps to quantify the change between the a priori and a posteriori distributions; higher values indicate better coverage of the input within the database and therefore a higher information content afforded by the retrieval. Relative entropy will be computed for various algorithm configurations

[1] Kullback and Leibler (1951) do not specify a logarithm base, but base 2 is adopted by convention to define information in units of a bit.

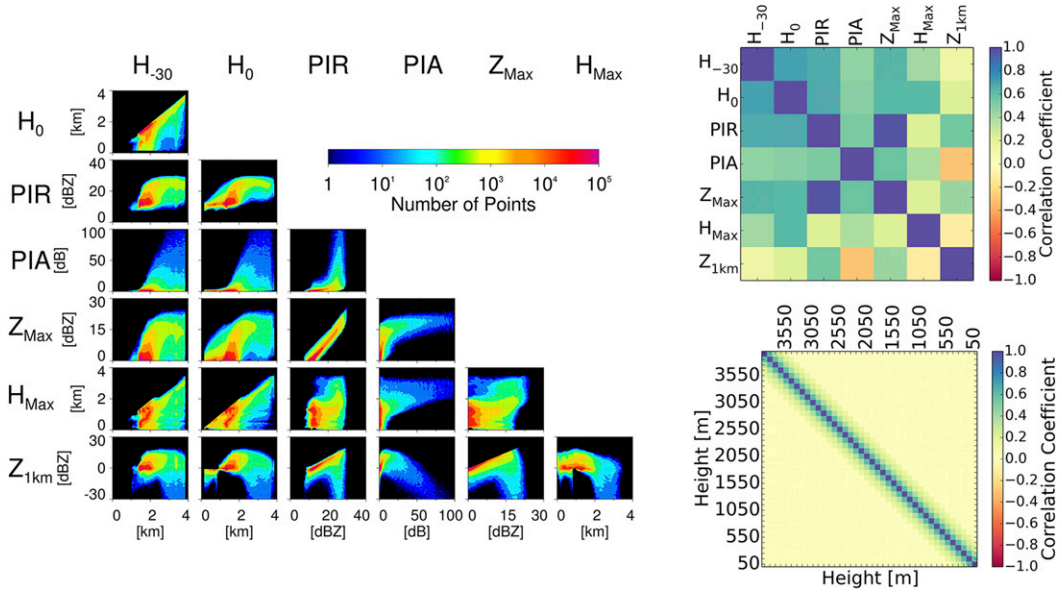

FIG. 2. (left) Two-dimensional histograms between different simulated reflectivity profile characteristics. (right) Correlation coefficients used in computing the covariance matrices of reflectivity parameters and for full reflectivity profile with an example functional decay with a scale length of 2 (see text).

relative to retrievals using only the 0-dBZ height. This parameter is chosen as a reference since all profiles in the database contain at least one bin with a reflectivity greater than or equal to 0 dBZ to ensure the presence of rain.

3. Model-based algorithm tests

To examine the behavior of the algorithm, a series of synthetic retrievals are conducted with cross sections and domains from model time steps that were not included in the retrieval database. Utilizing these excluded profiles provides test samples that are independent of the profiles included in the database. Initially, the full reflectivity profile at the model resolution is employed to provide a reference against which the performance of various parameter subsets at both model and *CloudSat* resolutions will be compared. Selected cross sections are examined qualitatively, while full domains are aggregated for statistical assessments of algorithm performance. The evaluation metrics described in section 2e are used throughout this process to guide the assessment.

a. Full-resolution retrievals

A sample retrieval for a cross section from the simulation with a 298-K SST and a maximum CCN of 400 cc^{-1} is shown in Fig. 3. In this scene, three precipitating cumulus clouds are present with the largest centered about 5 km from the western edge of the domain. The average latent heating profile shows cooling at cloud top [~2.2 km above ground level (AGL)] from entrainment and an area of heating through the middle extent of the cloud (2 km down to 800 m AGL) from condensational growth. Very slight cooling is occurring below the cloud base down to the surface owing to evaporative cooling in precipitation.

The full reflectivity profile is used to generate the estimates shown in Fig. 3. While the overall magnitudes of the retrieved quantities are generally consistent with the model truth, both the retrieved vertical profiles of latent heating (Fig. 3d) and column total latent heating and cooling (Fig. 3g) at the high native resolution of the RAMS simulations exhibit considerable noise across the domain. Retrieved LWP (Fig. 3f) is smoother and generally follows the trend of the model quantity. Surface rainfall rate (Fig. 3j) is also noisy and contains a peak of unrealistically high rainfall rate at 5 km, where the rate is almost 50% larger than the model value and then decreases to a much lower value. Latent heating estimates are also mismatched over 0–8 km from the left side, likely due to the close proximity of two cells combined with full attenuation of the reflectivity profile. While the mean statistics of the cross section are captured, this erratic behavior suggests that random errors are prevalent from profile to profile. Despite a high entropy (Fig. 3i), maximum probabilities (Fig. 3h) are near zero, meaning the retrieval does not fit the data very well.

The noisiness and poor fit of these full profile retrievals can be understood as follows: simulations used

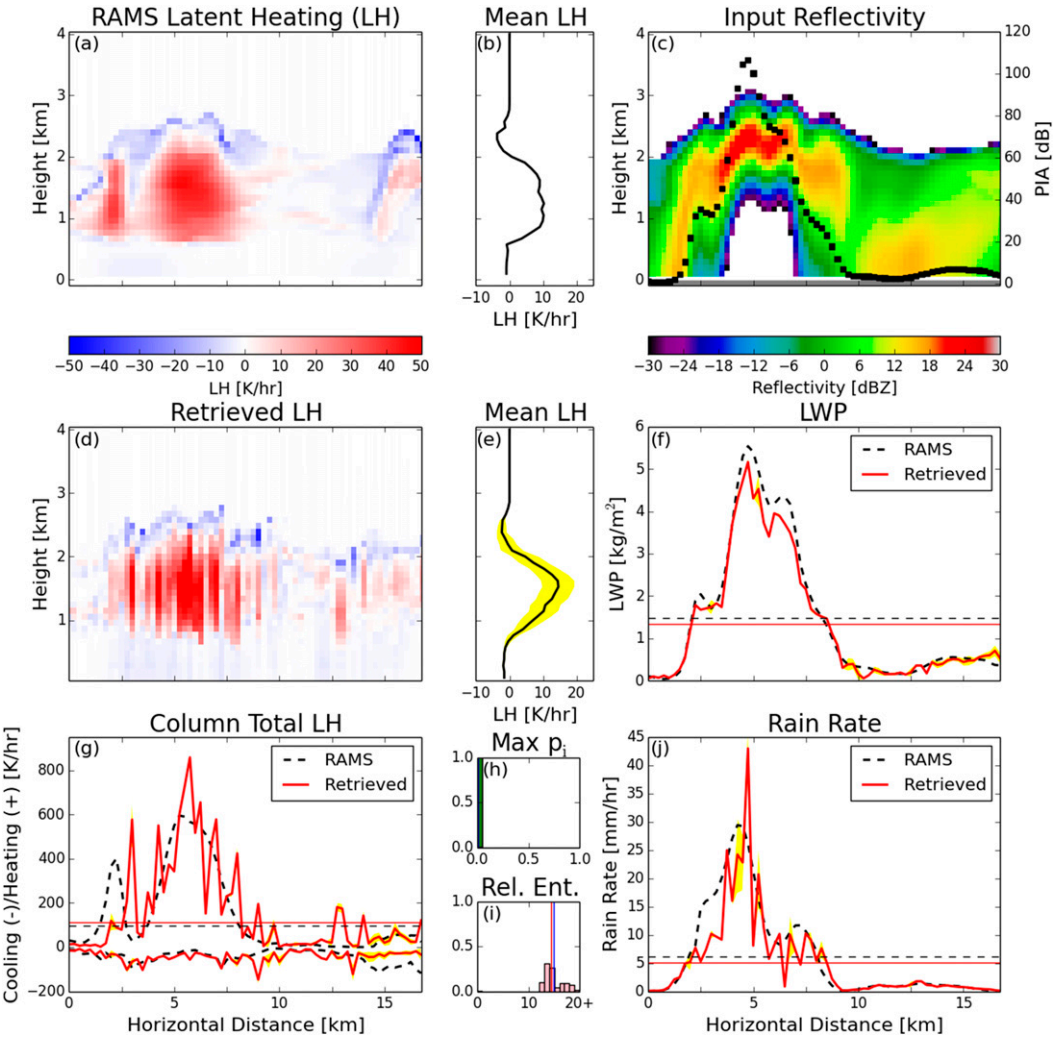

FIG. 3. Model resolution retrievals using the full reflectivity structure and PIA as the input, with error characteristics of $L_s = 2$, $\sigma_{\text{ref}} = 1$ dBZ, and $\sigma_{\text{att}} = 2$ dB. (a) Spatial distribution of latent heating from RAMS. (b) RAMS model average latent heating profile. (c) Input reflectivity shaded with PIA plotted in black. (d) Retrieved spatial distribution of latent heating. (e) Retrieved average latent heating profile with uncertainty shaded in yellow. (f) RAMS model (dashed black) and retrieved (solid red) LWP. (g) RAMS model and retrieved column total latent heating and latent cooling. (h) Distribution of maximum probability from each profile. (i) Relative entropy distribution from each profile. (j) RAMS model and retrieved surface rainfall rate. In (f), (g), and (j), the cross-sectional RAMS model and retrieval means are plotted as correspondingly styled horizontal lines [with (j) the combined heating and cooling]. In (h) and (i), the distribution mean (blue) and median (red) are plotted as vertical lines.

in the database provide discrete possible states of the atmosphere, not a continuous distribution fitted to observations or a theory that provides a relationship between two values. For the BMC retrieval to most effectively function, it requires a database that spans the complete state space for each dimension of observation. By constraining a database of discrete reflectivity profiles with accurate observations containing the same number of observational dimensions, areas of the distribution that do not fully span a given dimension will cause suboptimal behavior. The algorithm may isolate a profile at an extreme when it searches near the tail of the distribution. Because of this, the probability and spread are low and the retrieval devolves into a nearest-neighbor search. Furthermore, the low uncertainties that are retrieved are misleading. They do not indicate high confidence from the algorithm in the retrieval, but rather a lack of a sufficient number of close matches.

To smooth the discrete nature of the database, the spread of influence of each database member can be

increased by covariance matrix inflation. This can be accomplished by increasing either the assumed errors of an observation (σ_y) or the associated covariances between observations (r_{ij}). Assumed error increases can be attributed to accounting for other uncertainties in the real world. In the case of reflectivities, an example is the drop size distribution assumptions. The assumed error of the reflectivity bins is increased from 1 to 3 dBZ in Fig. 4a to investigate the effects of covariance inflation. Expanding the error allows more solutions to be considered and smooths some of the variations across the cross section. In Fig. 4b, the impacts of increasing the scale length of the reflectivity correlations from 2 to 6 are shown. This reduces the effective dimensionality of the profile by introducing stronger correlation relationships between a given reflectivity bin and its vertical neighbors. The distribution of retrieved latent heating is similar to that at the original scale length.

Using only covariance matrix inflation to relax the database for the maximum number of observables still results in a noisy retrieval that has a high spread of retrieval error and low algorithm confidence. This somewhat counterintuitive result suggests there may be value in using a smaller number of inputs for the algorithm, whose dimensionality is well captured by the database, to relax the discontinuous nature of the database. In other words, more observations do not necessarily result in a better retrieval, and increasing the degrees of freedom in the retrieval helps to smooth the state space of the database. The issue of overconstraining and a desire to reduce computation cost for a global retrieval both motivate exploring alternatives to using the full reflectivity profile. Important characteristics of the reflectivity profile, like those adopted in the SLH algorithm, are used in an attempt to collapse the profile into fewer observations while still capturing the signatures of the physical processes occurring.

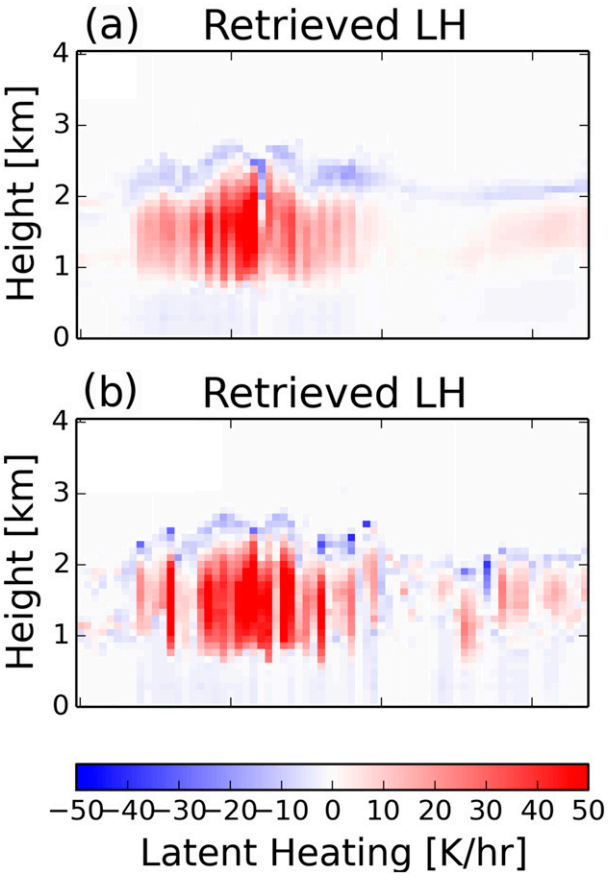

FIG. 4. Comparison of retrieved spatial latent heating distributions using the full reflectivity structure and PIA as the input with error characteristics of (a) $L_s = 2$, $\sigma_{\text{ref}} = 3$ dBZ, $\sigma_{\text{att}} = 2$ dB; and (b) $L_s = 6$, $\sigma_{\text{ref}} = 1$ dBZ, $\sigma_{\text{att}} = 2$ dB.

b. *Representativeness of the parameters*

First, to demonstrate the effects of different classes of profile characteristics on the retrieval and to qualify the choice of a mix of profile parameters, the seven input parameters described in section 2d are grouped into two categories. Parameters PIR, PIA, Z_M, and $Z_{1\text{km}}$ constrain cloud intensity and the amount of water within the column. Parameters H_{-30}, H_0, and H_M provide information about the structure of cloud and rain vertically. Figure 5 shows retrievals on the same cross section in Fig. 3, but for these subsets of parameters. At first glance, when using only the intensity parameters (Fig. 5i), the retrieved latent heating profiles are poorly constrained vertically. The tops of the clouds are ill defined and are situated at either 1 or 3 km, with higher tops in the greater rain-rate sections. All uncertainties are large except for those on LWP, but biases in column total latent heating, LWP, and rain rate are low. This demonstrates that integrated properties can constrain some of the bulk quantities even though the vertical distributions are misplaced.

When only the height values are used as algorithm input [Fig. 5(ii)], the vertical structure of the latent heating is retrieved with cloud tops and bases in reasonable agreement with model truth. Heating generally occurs in areas with reflectivity greater than 0 dBZ, and cooling occupies the area between the −30- and 0-dBZ heights. The average latent heating profile is better constrained with no heating or cooling above 3 km and a more marked vertical transition from overall heating to cooling. Column total latent heating, LWP, and rain rate are all, however, still significantly underestimated. Thus, the height parameters provide information on the vertical

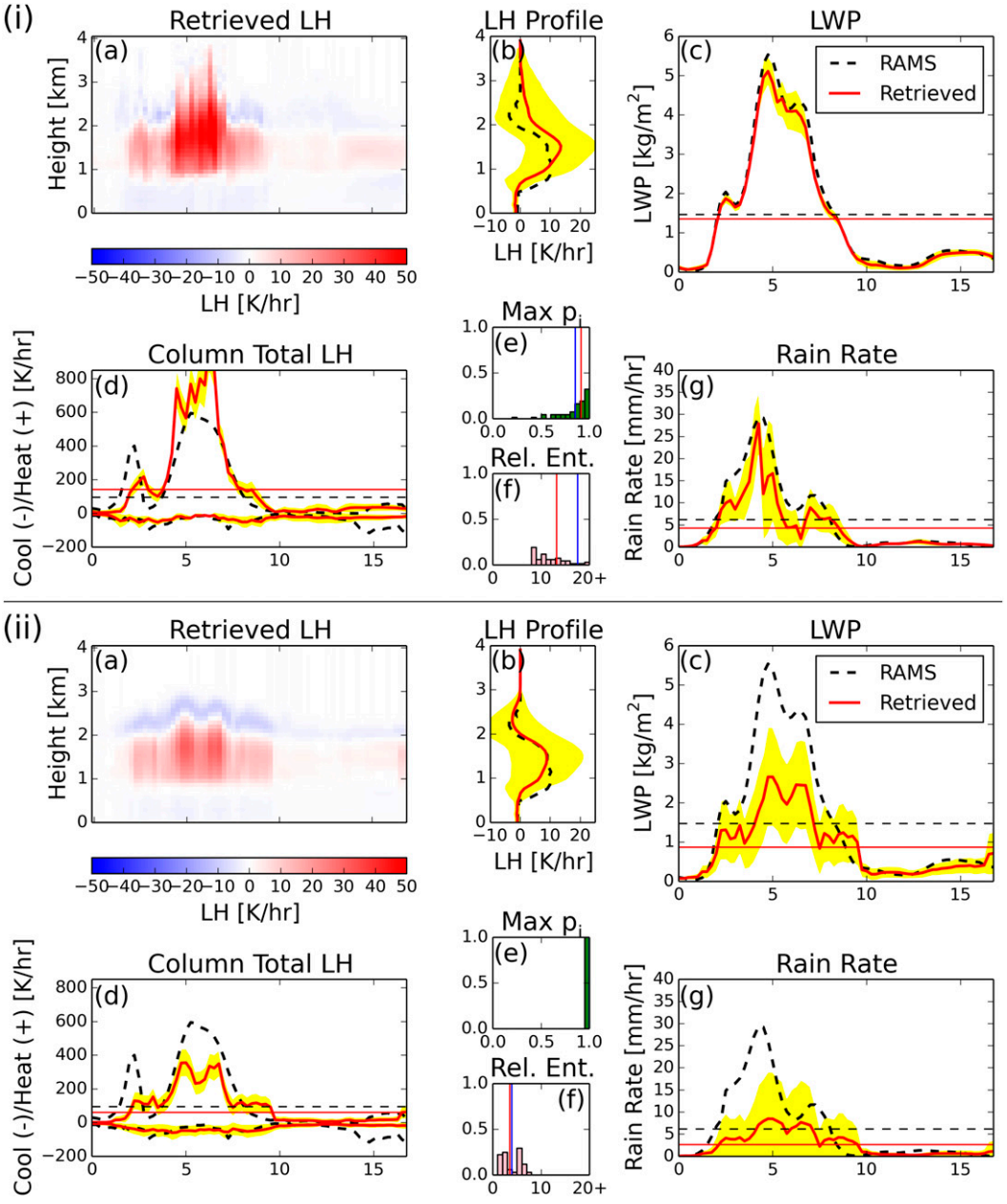

FIG. 5. Comparison of retrieved values using (i) the intensity category of parameters only with error characteristics of $\sigma_{\text{ref}} = 1$ dBZ, $\sigma_{\text{att}} = 2$ dB; and (ii) the height category of parameters only with error characteristics of $\sigma_{\text{hgt}} = 100$ m. (a)–(g) The same variables as in Figs. 3d–j.

distribution of heating but not the proper magnitude or intensity of any quantity.

c. *Conditioning the retrieval*

The preceding analysis demonstrates the synergy of including some height and some bulk intensity measures in the retrieval. To determine an optimal set of observations for the retrieval, combinations of parameters are analyzed in the context of information content metrics described in section 2e. The goal is to determine the minimum set of parameters that provides a high algorithm certainty while avoiding the stability issues described previously. Distributions of maximum probability and relative entropy are calculated for the retrieval over a full model domain not included in the database from the 298-K SST, 800 cc^{-1} CCN simulation. The algorithm is run with all possible combinations of parameters, and a sample of combinations with respective

maximum probability and relative entropy distributions is shown in Fig. 6. Recall that higher values of relative entropy for a given set of parameters indicate a greater increase in information relative to an algorithm that uses only the 0-dBZ height.

Adding only one or two variables to H_0 (top of Fig. 6) provides only modest increases in information content, while adding parameters related to intensity tends to provide more information. In cases where only a few parameters are included in the retrieval, the maximum probability distribution demonstrates that the database is able to fit the observations very well. By supplying just a few parameters as an input, the state space of these parameters is well sampled. The overall trend of the relative entropy shows that including up to six parameters increases the entropy gained while also retaining a good fit with maximum probabilities averaging near 0.75. When using all seven parameters examined (bottom of Fig. 6), mean maximum probabilities drop to 0.5 with only a minor increase in information when compared to six parameters. This is likely due to correlations between parameters that result in little information gain but lead to initial evidence that the database may undersample the measurement space of all seven parameters combined. Six parameters are, therefore, selected as optimal for this algorithm: H_{-30}, H_0, H_M, PIR, PIA, and $Z_{1\text{km}}$.

Figure 7 shows an application of the algorithm with these six chosen parameters to the cross section examined in Fig. 3. Heating within the largest cell is retrieved with cooling at the top of the cloud. The secondary cell to the left is also captured by the algorithm, with a slightly shallower layer of heating and associated cooling above the cloud. Cooling consistent with evaporation also appears below the cloud base, with stronger cooling corresponding to the more intense part of the largest cell. Finally, the dissipating cell on the right edge of the cross section exhibits shallow heating centered vertically around 1.5 km and cooling near the top of the cloud. The average latent heating profile captures heating through the middle extent of the cloud and the peak near 1.8 km. Cooling above about 2 km corresponds to the entrainment cooling that occurs at the same level in the model truth. The retrieved average profile is slightly more peaked than the truth, but the uncertainty in the profile captures the truth values.

There is excellent agreement between the model and the retrieved LWP (Fig. 7f), with the model mean slightly underestimated by the retrieval. Column total latent heating (Fig. 7g) reproduces the broad features of the cross section well and profile-to-profile noise has been reduced compared to the full profile retrieval (Fig. 3). Strong heating from the largest cell is captured as is the weaker heating between the two clusters of cells horizontally at 10–13 km from the left. Retrieved cooling is not as strong in the far right cell or between the two left cells, but that is compensated for by some underestimation of heating and cooling in other areas, resulting in very little bias in the domain-averaged column total latent heating retrievals. Finally, the broad features of the surface rainfall rate (Fig. 7j) are captured with both regions of more intense rainfall and very light rain near the dissipating cell.

d. *Impact of spatial resolution*

The ultimate goal of this work is to develop an approach that can be applied to *CloudSat* observations that have reduced resolution compared to the native model resolution considered thus far. To explore the impact of coarser spatial resolution, the CRM database is degraded to the 1.5-km spatial and 300-m vertical resolutions appropriate for the *CloudSat* CPR. Data in the lowest three bins (up to 700 m) are removed to simulate the effects of ground clutter in *CloudSat* observations. Figure 8 shows that the two leftmost cells merge into one large area of heating and that the dissipating cell at 13–17 km from the left edge is reduced to an area of primarily upper-level cooling as a result of this resolution degradation. The average RAMS profile is slightly smoother than in Fig. 7 with peak cooling due to cloud-top entrainment near 2.3 km AGL, heating through much of the 2–1-km AGL layer, and slight evaporative cooling below the cloud base. Magnitudes in the average latent heating profile are very similar to those of Fig. 7 with close to 10 K h^{-1} in the heating core.

The retrieved and average profiles of latent heating in Figs. 8d,e agree fairly well with the modeled latent heating as peaks in the average vertical profile match those of the truth, with the uncertainty in the profile again capturing the model profile. The retrieved LWP (Fig. 8f) nearly matches the model truth, similar to the performance of the algorithm at full model resolution. Column total latent heating (Fig. 8g) is biased slightly higher, but the spatial distribution is well captured. While the rain-rate structure is captured, the average across the cross section is biased low. Compared to the native model resolution results, the degraded reflectivity structure misses many of the previous features due to both spatial averaging and the simulated ground contamination. Thus, as one would expect, decreased resolution blurs many of the finer-scale features, but these results suggest that degrading the resolution does not substantially decrease algorithm performance and that the algorithm input parameters provide sufficient

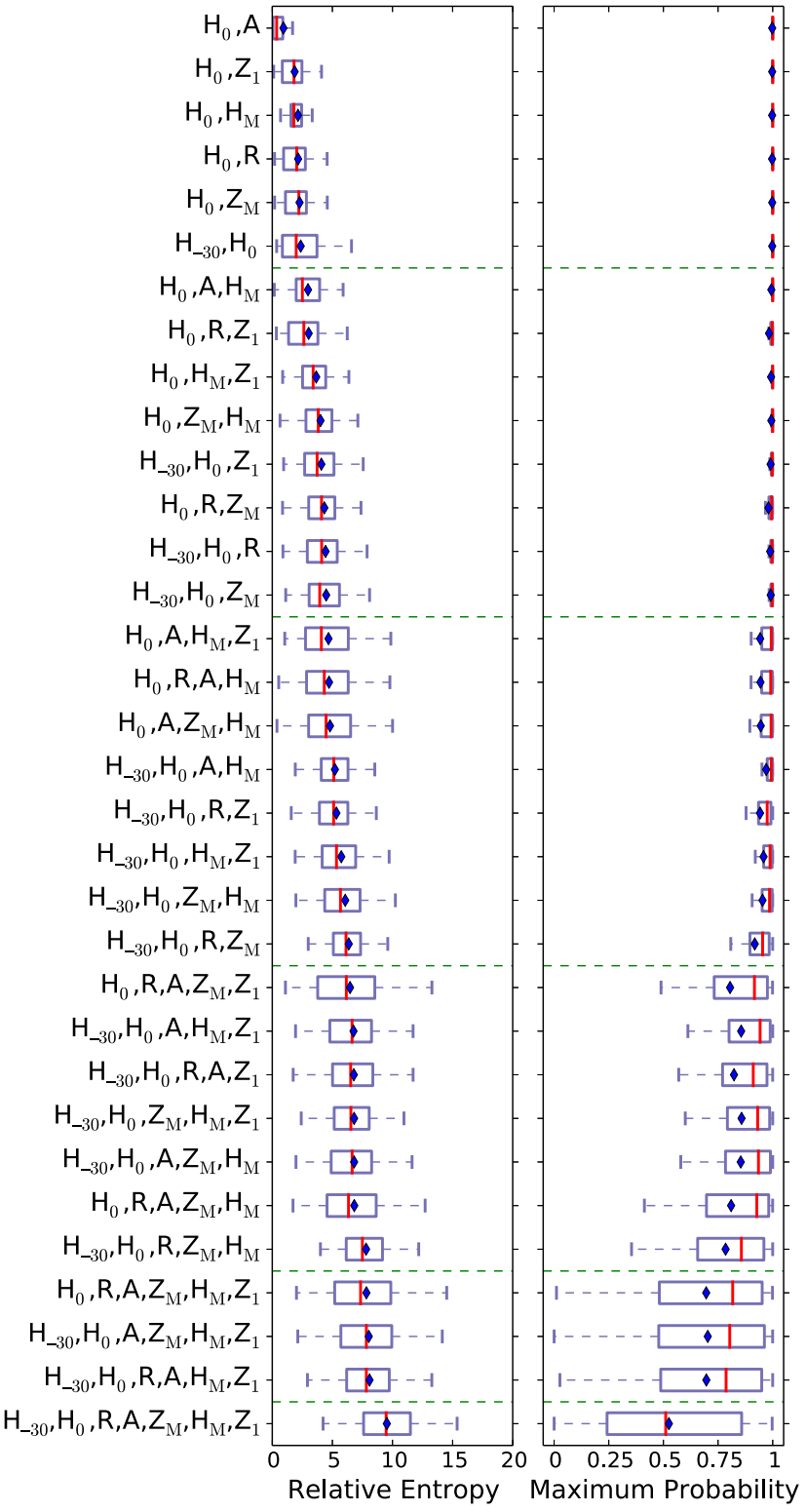

FIG. 6. Relative entropy and maximum unnormalized probability distributions on a full output domain for multiple algorithm parameter combinations relative to the 0-dBZ height retrieval. The blue diamond indicates the distribution mean, and the red line indicates the distribution median. The left (right) box edge is the 25th (75th) percentile, with the box width defined as the interquartile range (IQR). The left (right) whisker is the 25% − IQR (75% + IQR) value.

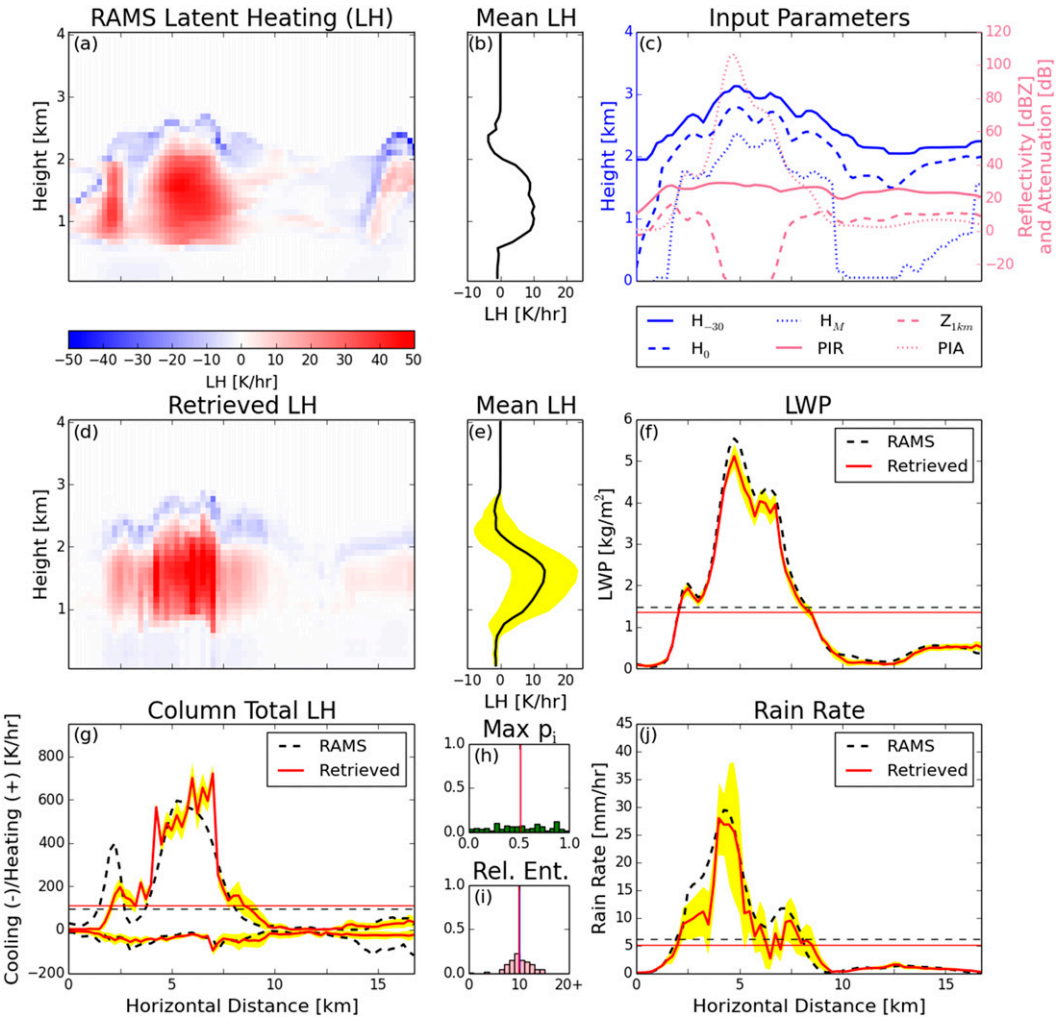

FIG. 7. As in Fig. 3, but using the algorithm reflectivity profile parameters as input—H_{-30}, H_0, H_M, PIR, PIA, and $Z_{1\mathrm{km}}$—with errors of $\sigma_{\mathrm{ref}} = 1\,\mathrm{dB}Z$, $\sigma_{\mathrm{att}} = 2\,\mathrm{dB}$, and $\sigma_{\mathrm{hgt}} = 100\,\mathrm{m}$.

information to perform physically reasonable latent heating retrievals.

e. Retrieval performance

To provide a more statistical assessment of retrieval performance, retrieved LWP, surface rainfall rate, and total column latent heating and cooling from a full 298-K SST, $800\,\mathrm{cc}^{-1}$ CCN simulation time step at both the model and *CloudSat* resolutions are compared against the model truth in Fig. 9. For the model resolution, LWP is retrieved very well, with the scatterplot following a 1:1 ratio between modeled and retrieved values. The domain LWP bias is $-9.3 \times 10^{-5}\,\mathrm{kg\,m^{-2}}$ (-0.02%) and the root-mean-square error (RMSE) is $0.1\,\mathrm{kg\,m^{-2}}$. Rainfall-rate retrievals are biased $-0.09\,\mathrm{mm\,h^{-1}}$ (-8.7%) and have an RMSE of $1.5\,\mathrm{mm\,h^{-1}}$. At lower rainfall rates, the retrieval approximately straddles a 1:1 ratio, while higher rainfall rates are biased low, which is likely due to attenuation. Latent heating and cooling tend to be biased low, where latent heating has a negative bias ($-25.14\,\mathrm{K\,h^{-1}}$; -35.2%) and the latent cooling has a positive bias ($25.25\,\mathrm{K\,h^{-1}}$; 54.6%). When these two components are summed together, the bias in total latent heat release across the domain is negligible. Biases in the retrieved level of maximum latent heating and cooling are within about one vertical level, indicating the algorithm does an excellent job of characterizing the vertical distribution of processes in the column.

Averaging the test output time from native resolution to contiguous *CloudSat* profiles provides only a small number of samples—less than 3% of the model resolution test. To achieve a reasonable sample size for meaningful statistics, every single profile in this domain is averaged with its respective neighboring profiles to

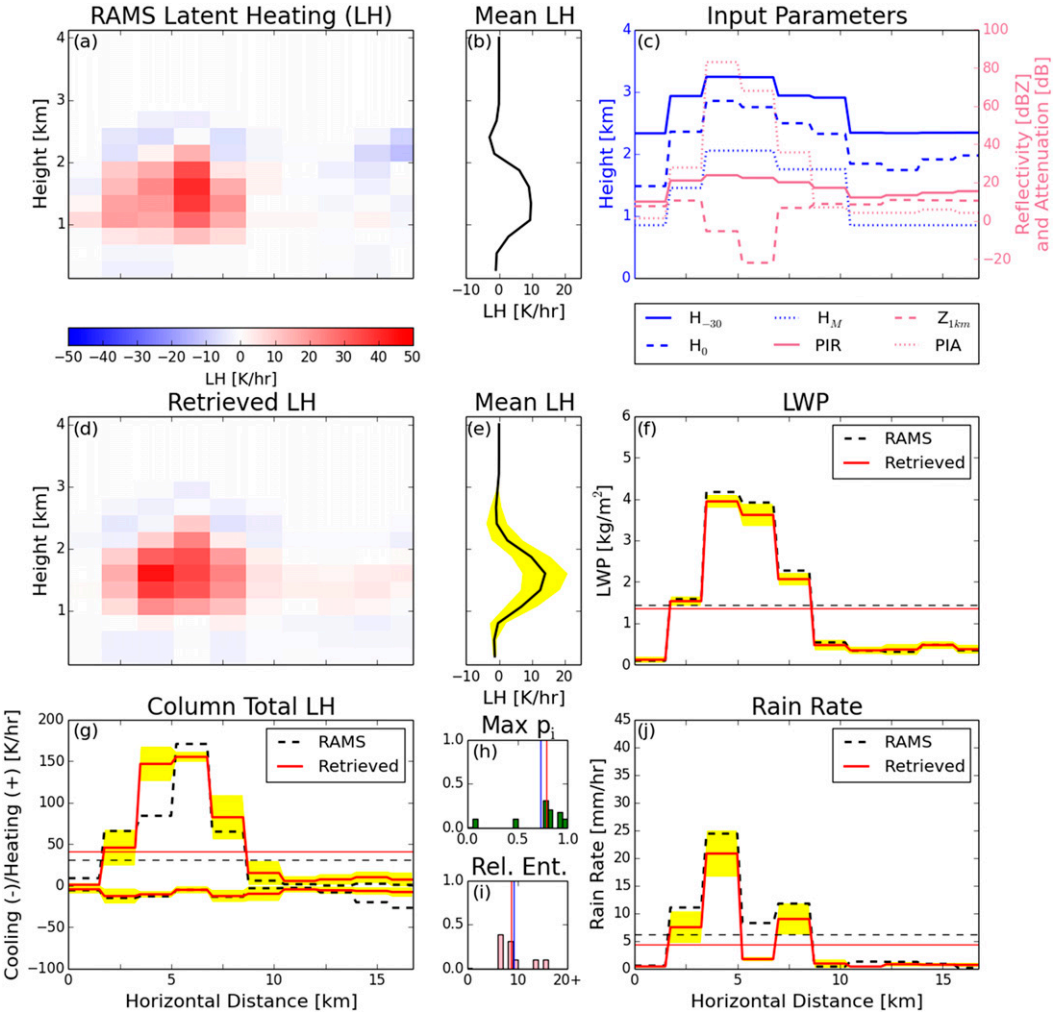

FIG. 8. As in Fig. 7, but using the algorithm reflectivity profile parameters at *CloudSat* resolution with errors of $\sigma_{\text{ref}} = 1\,\text{dB}Z$, $\sigma_{\text{att}} = 2\,\text{dB}$, and $\sigma_{\text{hgt}} = 300\,\text{m}$.

the *CloudSat* resolution. This process simulates a Monte Carlo sampling of footprint configurations in the test domain at *CloudSat* resolution while removing any subjective choice as to which profiles serve as the footprint centers. Moreover, to replicate the temporal implications of integrating over an area, outputs from three consecutive model time steps are averaged together to provide time-mean values of the retrieved properties. Figure 10 shows the results from this test.

At the decreased resolution, LWP continues to be well captured with a bias of $-0.01\,\text{kg}\,\text{m}^{-2}$ (-2.7%) and an RMSE of $0.04\,\text{kg}\,\text{m}^{-2}$. Rainfall-rate biases are reduced to $-0.01\,\text{mm}\,\text{h}^{-1}$ (-2.6%) and an RMSE of $0.6\,\text{mm}\,\text{h}^{-1}$. Latent heating and cooling are again biased as was the case at the model resolution; heating has a $-2.44\,\text{K}\,\text{h}^{-1}$ (-23.5%) bias while cooling has a $3.03\,\text{K}\,\text{h}^{-1}$ (51.6%) bias. Summing the total heating and cooling yields a domain, time-averaged bias of $0.6\,\text{K}\,\text{h}^{-1}$. The heights of maximum heating and cooling are captured extremely well with negligible biases of 0.3 m (0.9%) and −4.3 m (−14.8%), respectively.

These statistics show that the algorithm can successfully retrieve LWP, surface rainfall rate, and both the bulk latent heating and the vertical structure for full domains not included in the database. Algorithm performance is reasonably consistent between the native resolution of the model and the decreased *CloudSat* resolutions.

4. Application to observations

To illustrate the potential value of the algorithm for real-world applications, two classes of observations are chosen that approximately match the two spatial

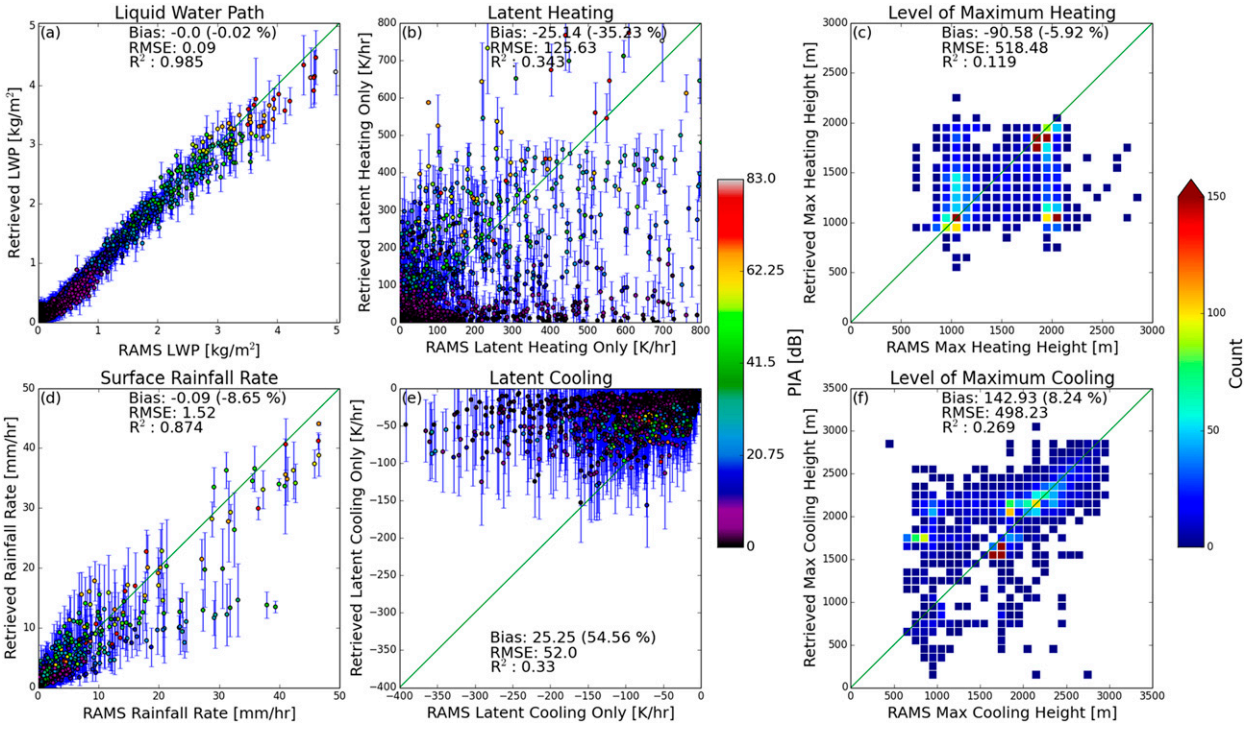

FIG. 9. LWP, surface rainfall rate, latent heating and cooling, and levels of maximum latent heating and cooling scatterplots between RAMS and the retrieval on a full domain at model resolution. LWP, surface rainfall rate, latent heating, and latent cooling points are shaded by PIA of the profile, while levels of maximum heating and cooling are shaded by the number of profiles within each plotted bin. A line of equality is plotted in green for reference.

resolutions explored before. Aircraft radar observations from the Variability of American Monsoon Systems (VAMOS) Ocean–Cloud–Atmosphere–Land Study (VOCALS) campaign resemble the model resolution database, while application to *CloudSat* observations demonstrates the results from application to coarser-resolution measurements.

a. VOCALS

VOCALS was an international study to determine the mechanisms and impact of aerosol indirect effects in the southeastern Pacific Ocean and to improve atmospheric and coupled atmosphere–ocean models in this area (Mechoso et al. 2014). Part of VOCALS was a field campaign called the VOCALS Regional Experiment (VOCALS-REx) that conducted intensive ship-based, aerial, and land-based observations, including radar, radiosonde, and aerosol measurements. One of the participating aircraft was the NSF/NCAR C-130 equipped with the Wyoming Cloud Radar, a 94-GHz (W band) radar that operated at a resolution of approximately 3.5 m horizontally and 15 m vertically, with a noise estimate of 3 dBZ (Oolman and Leon 2009).

On 2 November 2008, the C-130 flew over a pocket of open cellular convection, taking a cross section highlighting shallow convection of varying intensity. No attenuation information was available because of the varied flight height, so the retrieval is performed without PIA and with $\sigma_{\text{ref}} = 3\,\text{dB}Z$ due to the increased instrument noise. Figure 11 displays the scene and retrieval results. The algorithm shows three cores of precipitation from 2–4, 8–10, and 13–15 km horizontally. LWPs (Fig. 11f) for these regions are $\sim 1\,\text{kg}\,\text{m}^{-2}$, with the highest LWPs corresponding to the areas of maximum rainfall rate. Retrieved latent heating profiles (Fig. 11d) show strong heating in the levels of maximum reflectivity from precipitation formation and cooling occurring in areas where water drops are likely evaporating. The large uncertainties in all retrieved quantities are likely due to the absence of PIA.

This VOCALS retrieval example demonstrates that the algorithm can be used to provide realistic latent heating estimates from airborne cloud radar observations at a finer resolution than that available from satellite-based radars. It also shows that the database contains sufficient diversity to capture the variability observed in this scene. This highlights the flexibility of the algorithm, as the parameters chosen can be obtained from any radar provided it exhibits sufficient

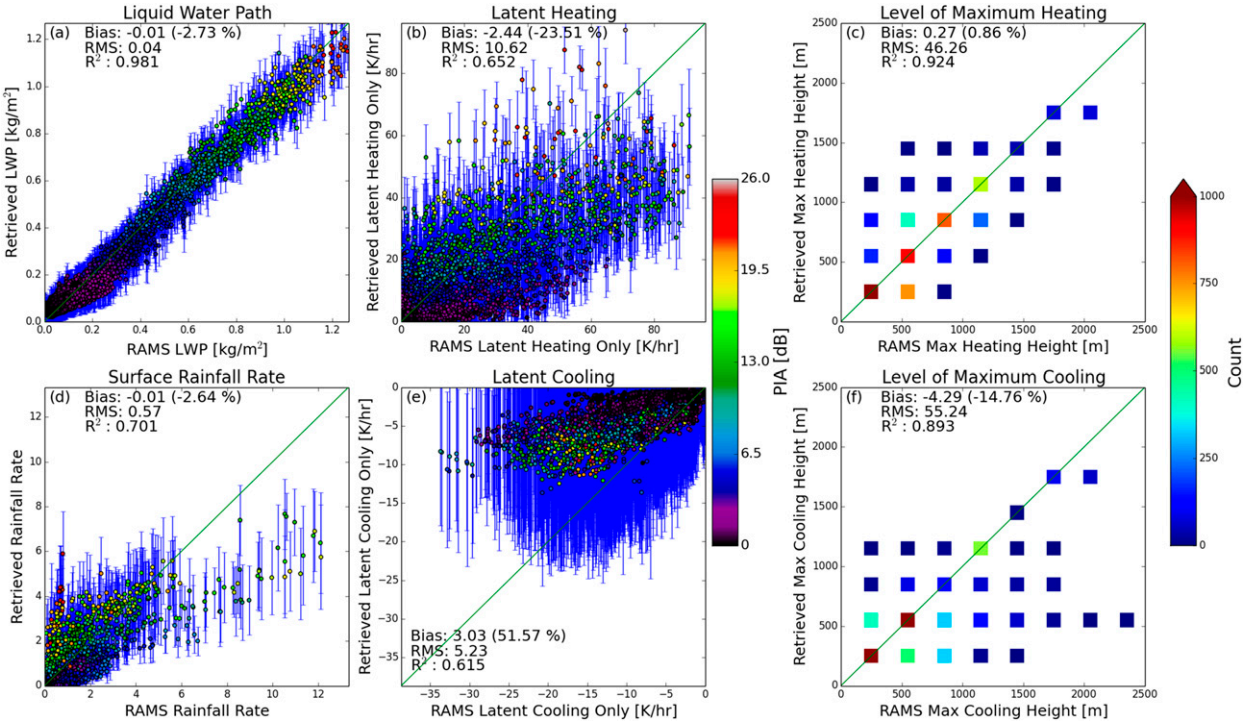

FIG. 10. As in Fig. 9, but for the *CloudSat* resolution algorithm database and time averaged over 15 min.

sensitivity to derive the required −30- and 0-dBZ heights. Therefore, the algorithm is not platform specific.

b. CloudSat

Next, the retrieval is applied to a shallow tropical raining scene observed by *CloudSat* in granule 3585, which passed over the central Pacific Ocean on 30 December 2006. Reflectivities are taken directly from the 2B-GEOPROF product, while attenuation values are chosen to be the two-way near-surface bin attenuation estimates from 2C-PRECIP-COLUMN (CloudSat Data Processing Center 2007). The retrieval for a section of this granule is shown in Fig. 12.

Through the extent of the swath, areas of strong reflectivity and higher PIA coincide with high rainfall rates and high LWPs. The spatial pattern of latent heating is consistent with physical expectations: heating is strongest in areas that feature taller reflectivity cores that correspond to deeper rainfall-generating cells. Cooling occurs at the cloud top indicative of entrainment of drier air. Furthermore, relatively strong cooling exists below the cloud base in areas where the highest surface rainfall rates are retrieved, indicating that a higher flux of rainwater provides more water to be evaporated. Once again, latent heating cannot be directly evaluated, but in this case we can compare retrieved surface rainfall rates to the existing *CloudSat* rainfall products. Doing so shows agreement through most of the cross section, with some heavier rainfall present in areas of deeper profiles and an underestimation in the 10–20-km range from the left side where little heating is retrieved. As a whole, the algorithm retrieves quantities that are consistent with other *CloudSat* granule products.

5. Conclusions and forthcoming work

There remains a gap in our understanding of the global role of latent heating in warm rain systems partly due to a lack of observations of light precipitation and shallow clouds from conventional precipitation sensors. The BMC algorithm presented here provides a pathway to filling this need by relating characteristics of radar reflectivity profiles to the associated microphysical processes and, in turn, resulting latent heating structure, LWP, and surface rainfall rate in warm rain scenes. Information about cloud vertical extent is provided by H_{-30}, H_0, and H_M, while the bulk properties are constrained with PIR, PIA, and $Z_{1\text{km}}$. By using these characteristics instead of the full reflectivity profile, computation time is reduced and problems associated with large dimensionality in the database construction are mitigated. Furthermore, the BMC approach is readily adaptable to different platforms

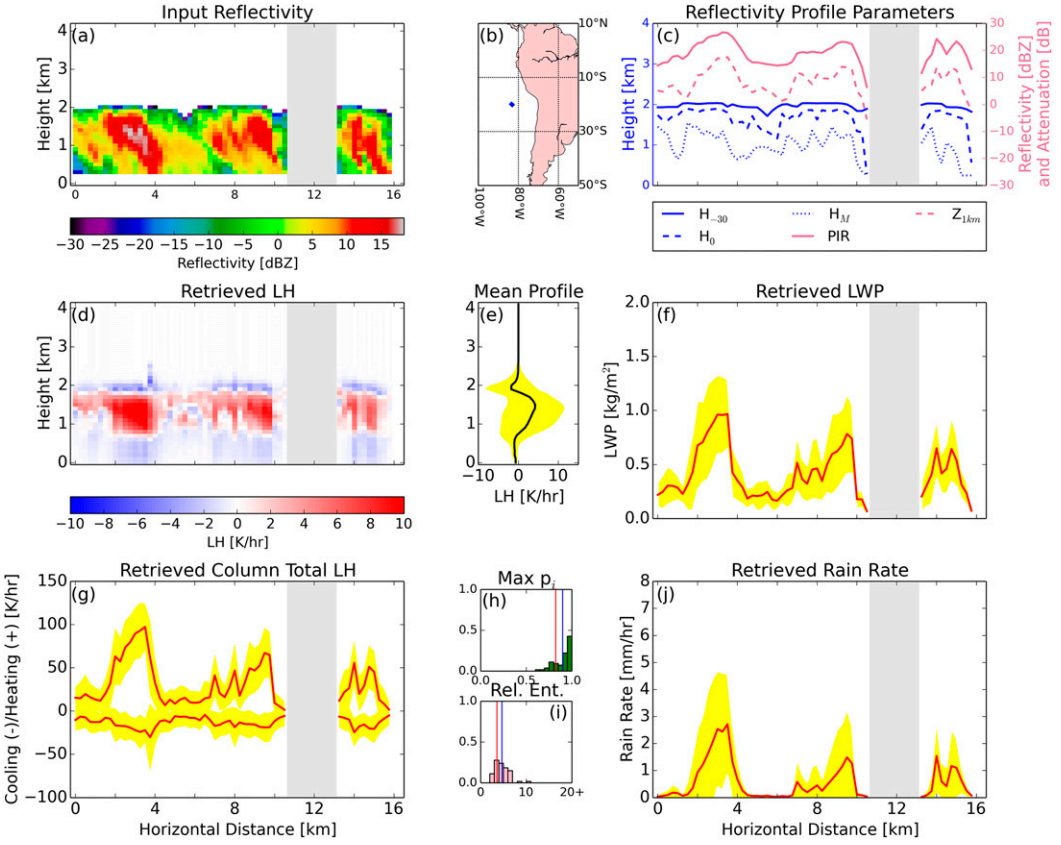

FIG. 11. Model resolution retrieval of the test algorithm on a section of C-130 Wyoming Cloud Radar data from the VOCALS campaign on 2 Nov 2008. (a) Input reflectivity structure. The gap corresponds to a portion of the cross section with no reflectivity exceeding 0 dBZ. (b) Map displaying location of section. (c) Reflectivity profile parameters calculated from input reflectivity. (d) Retrieved spatial distribution of latent heating, (e) average latent heating profile, (f) LWP, and (g) column total latent heating and cooling. (h) Maximum probability and (i) relative entropy distributions. (j) Retrieved surface rainfall rate. (Data courtesy of Larry Oolman and David Leon, University of Wyoming.)

and provides a framework for including additional measurements from other sources in the future.

At model resolution, domain-averaged biases are low despite large RMSE, an indication that retrieval accuracy is dominated by random error. Upscaling the algorithm to *CloudSat* resolution yields similar results in retrieval performance. The algorithm was applied to observations collected during VOCALS and by *CloudSat*, yielding realistic structures of latent heating, LWP, and surface rainfall rates. The diversity of observation sources demonstrates that the algorithm is not tied to a specific instrument or platform, but that it can be applied to any observations from which the algorithm inputs can be derived. Yet the ability of the algorithm to provide distinguishing information for light precipitation is reliant on the resolution and scale of the observation. In the analysis performed here, the most intense areas of heating ranged from a horizontal scale of 2 to 10 km, and some of the highest reflectivities were only near 15 dBZ. Future observing platforms seeking to estimate the characteristics of warm rain should consider the scale necessary to observe these features.

To expand the algorithm to other cloud morphologies that include ice-phase processes, additional model simulations are required to supplement the algorithm database. Furthermore, such an application to other cloud types or instruments will require additional assessments of the forward model contributions to the error covariance matrices chosen. This assessment can be accomplished by propagating uncertainties in all assumptions through the algorithm and quantifying the resulting changes in retrieved latent heating profiles. Retrieving other precipitation regimes may also warrant a dynamic error covariance matrix that varies depending on the location and environment of the algorithm input.

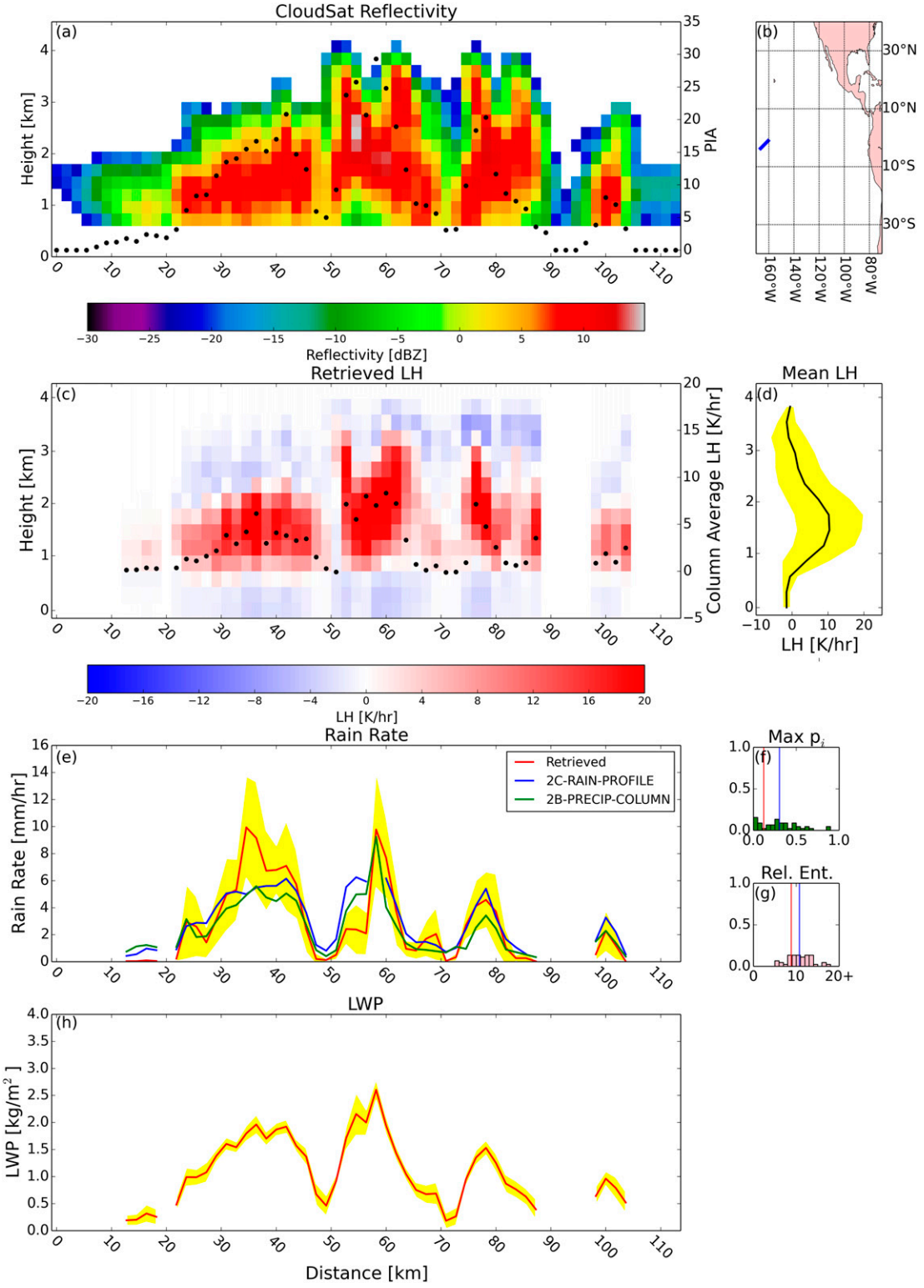

FIG. 12. The first attempt at a warm rain latent heating retrieval from *CloudSat* observations. This scene is from granule 3585 observed on 30 Dec 2006. (a) Reflectivity structure and two-way PIA from 2B-GEOPROF and 2C-PRECIP-COLUMN near-surface bin attenuation product, respectively. (b) Map displaying location and orientation of the section with the length of the line exaggerated to show detail. (c) Retrieved spatial distribution of latent heating. (d) Retrieved average latent heating profile. (e) Retrieved surface rainfall rate with uncertainty shaded in yellow. 2C-RAIN-PROFILE (blue) and 2B-PRECIP-COLUMN (green) rainfall-rate products are included for comparison. Distributions of (f) maximum probability and (g) relative entropy. (h) Retrieved LWP. (Data courtesy of the CloudSat Data Processing Center.)

The BMC approach utilized in this paper offers a method for processing the complete *CloudSat* archive to create a new shallow latent heating product. This dataset could provide new insights into the spatial and temporal distributions of latent heating from warm rain systems globally. Moreover, the potential to combine *CloudSat*'s estimates of latent heating from light precipitation with those in heavier precipitation from TRMM and the Global Precipitation Measurement paves the way for a more complete perspective of latent heating within the tropical regions of the atmosphere. Finally, the portability of the algorithm provides the opportunity for it to be used on future missions that can sense light precipitation, like the Earth Clouds, Aerosol and Radiation Explorer (EarthCARE) satellite (Illingworth et al. 2015).

Acknowledgments. This work was supported by NASA *CloudSat*/*CALIPSO* Science Team Grant NNX13AQ32G, the NASA ACE Grant NNX13AK08G, and NASA Headquarters under the NASA Earth and Space Science Fellowship Program Grant NNX14AL35H. VOCALS data were courtesy of Larry Oolman and David Leon (University of Wyoming) and provided by NCAR/EOL under sponsorship of the National Science Foundation (http://data.eol.ucar.edu/). *CloudSat* data were obtained through the *CloudSat* Data Processing Center (http://www.cloudsat.cira.colostate.edu).

REFERENCES

Aubert, E. J., 1957: On the release of latent heat as a factor in large scale atmospheric motions. *J. Meteor.*, **14**, 527–542, doi:10.1175/1520-0469(1957)014<0527:OTROLH>2.0.CO;2.

Berg, W., T. L'Ecuyer, and J. M. Haynes, 2010: The distribution of rainfall over oceans from spaceborne radars. *J. Appl. Meteor. Climatol.*, **49**, 535–543, doi:10.1175/2009JAMC2330.1.

CloudSat Data Processing Center, 2007: CloudSat level 2 and level 3 data, release 4. Cooperative Institute for Research in the Atmosphere, accessed 20 September 2012. [Available online at http://www.cloudsat.cira.colostate.edu/data-products.]

Cotton, W. R., and Coauthors, 2003: RAMS 2001: Current status and future directions. *Meteor. Atmos. Phys.*, **82**, 5–29, doi:10.1007/s00703-001-0584-9.

Ellis, T. D., T. L'Ecuyer, J. M. Haynes, and G. L. Stephens, 2009: How often does it rain over the global oceans? The perspective from CloudSat. *Geophys. Res. Lett.*, **36**, L03815, doi:10.1029/2008GL036728.

Evans, K. F., J. Turk, T. Wong, and G. L. Stephens, 1995: A Bayesian approach to microwave precipitation profile retrieval. *J. Appl. Meteor.*, **34**, 260–279, doi:10.1175/1520-0450-34.1.260.

Guimond, S. R., and J. M. Reisner, 2012: A latent heat retrieval and its effects on the intensity and structure change of Hurricane Guillermo (1997). Part II: Numerical simulations. *J. Atmos. Sci.*, **69**, 3128–3146, doi:10.1175/JAS-D-11-0201.1.

——, M. A. Bourassa, and P. D. Reasor, 2011: A latent heat retrieval and its effects on the intensity and structure change of Hurricane Guillermo (1997). Part I: The algorithm and observations. *J. Atmos. Sci.*, **68**, 1549–1567, doi:10.1175/2011JAS3700.1.

Hagos, S., and Coauthors, 2010: Estimates of tropical diabatic heating profiles: Commonalities and uncertainties. *J. Climate*, **23**, 542–558, doi:10.1175/2009JCLI3025.1.

Hartmann, D. L., H. H. Hendon, and R. A. Houze, 1984: Some implications of the mesoscale circulations in tropical cloud clusters for large-scale dynamics and climate. *J. Atmos. Sci.*, **41**, 113–121, doi:10.1175/1520-0469(1984)041<0113:SIOTMC>2.0.CO;2.

Haynes, J. M., and G. L. Stephens, 2007: Tropical oceanic cloudiness and the incidence of precipitation: Early results from CloudSat. *Geophys. Res. Lett.*, **34**, L09811, doi:10.1029/2007GL029335.

——, Z. Luo, G. L. Stephens, R. T. Marchand, and A. Bodas-Salcedo, 2007: A multipurpose radar simulation package: QuickBeam. *Bull. Amer. Meteor. Soc.*, **88**, 1723–1727, doi:10.1175/BAMS-88-11-1723.

——, T. S. L'Ecuyer, G. L. Stephens, S. D. Miller, C. Mitrescu, N. B. Wood, and S. Tanelli, 2009: Rainfall retrieval over the ocean with spaceborne W-band radar. *J. Geophys. Res.*, **114**, D00A22, doi:10.1029/2008JD009973.

Houze, R. A., 1982: Cloud clusters and large-scale vertical motions in the tropics. *J. Meteor. Soc. Japan*, **60**, 396–410.

Illingworth, A. J., and Coauthors, 2015: The EarthCARE satellite: The next step forward in global measurements of clouds, aerosols, precipitation, and radiation. *Bull. Amer. Meteor. Soc.*, **96**, 1311–1332, doi:10.1175/BAMS-D-12-00227.1.

Jiang, X., and Coauthors, 2009: Vertical heating structures associated with the MJO as characterized by TRMM estimates, ECMWF reanalyses, and forecasts: A case study during 1998/99 winter. *J. Climate*, **22**, 6001–6020, doi:10.1175/2009JCLI3048.1.

——, and Coauthors, 2011: Vertical diabatic heating structure of the MJO: Intercomparison between recent reanalyses and TRMM estimates. *Mon. Wea. Rev.*, **139**, 3208–3223, doi:10.1175/2011MWR3636.1.

Johnson, R. H., and P. E. Ciesielski, 2000: Rainfall and radiative heating rates from TOGA COARE atmospheric budgets. *J. Atmos. Sci.*, **57**, 1497–1514, doi:10.1175/1520-0469(2000)057<1497:RARHRF>2.0.CO;2.

——, T. M. Rickenbach, S. A. Rutledge, P. E. Ciesielski, and W. H. Schubert, 1999: Trimodal characteristics of tropical convection. *J. Climate*, **12**, 2397–2418, doi:10.1175/1520-0442(1999)012<2397:TCOTC>2.0.CO;2.

Kullback, S., and R. A. Leibler, 1951: On information and sufficiency. *Ann. Math. Stat.*, **22**, 79–86, doi:10.1214/aoms/1177729694.

Kummerow, C., and L. Giglio, 1994: A passive microwave technique for estimating rainfall and vertical structure information from space. Part I: Algorithm description. *J. Appl. Meteor.*, **33**, 3–18, doi:10.1175/1520-0450(1994)033<0003:APMTFE>2.0.CO;2.

——, W. Barnes, T. Kozu, J. Shiue, and J. Simpson, 1998: The Tropical Rainfall Measuring Mission (TRMM) sensor package. *J. Atmos. Oceanic Technol.*, **15**, 809–817, doi:10.1175/1520-0426(1998)015<0809:TTRMMT>2.0.CO;2.

L'Ecuyer, T. S., and G. L. Stephens, 2002: An uncertainty model for Bayesian Monte Carlo retrieval algorithms: Application to the TRMM observing system. *Quart. J. Roy. Meteor. Soc.*, **128**, 1713–1737, doi:10.1002/qj.200212858316.

——, and J. H. Jiang, 2010: Touring the atmosphere aboard the A-Train. *Phys. Today*, **63**, 36–41, doi:10.1063/1.3463626.

Lebsock, M. D., and T. S. L'Ecuyer, 2011: The retrieval of warm rain from CloudSat. *J. Geophys. Res.*, **116**, D20209, doi:10.1029/2011JD016076.

Lin, B., and W. B. Rossow, 1997: Precipitation water path and rainfall rate estimates over oceans using special sensor microwave imager and International Satellite Cloud Climatology Project data. *J. Geophys. Res.*, **102**, 9359–9374, doi:10.1029/96JD03987.

Liu, C., and E. J. Zipser, 2009: "Warm rain" in the tropics: Seasonal and regional distributions based on 9 yr of TRMM data. *J. Climate*, **22**, 767–779, doi:10.1175/2008JCLI2641.1.

Mapes, B. E., and R. A. Houze Jr., 1993: An integrated view of the 1987 Australian monsoon and its mesoscale convective systems. Part II: Vertical structure. *Quart. J. Roy. Meteor. Soc.*, **119**, 733–754, doi:10.1002/qj.49711951207.

——, P. E. Ciesielski, and R. H. Johnson, 2003: Sampling errors in rawinsonde-array budgets. *J. Atmos. Sci.*, **60**, 2697–2714, doi:10.1175/1520-0469(2003)060<2697:SEIRB>2.0.CO;2.

McCumber, M., W.-K. Tao, J. Simpson, R. Penc, and S.-T. Soong, 1991: Comparison of ice-phase microphysical parameterization schemes using numerical simulations of tropical convection. *J. Appl. Meteor.*, **30**, 985–1004, doi:10.1175/1520-0450-30.7.985.

Mechoso, C. R., and Coauthors, 2014: Ocean–cloud–atmosphere–land interactions in the southeastern Pacific: The VOCALS program. *Bull. Amer. Meteor. Soc.*, **95**, 357–375, doi:10.1175/BAMS-D-11-00246.1.

Olson, W. S., C. D. Kummerow, Y. Hong, and W.-K. Tao, 1999: Atmospheric latent heating distributions in the Tropics derived from satellite passive microwave radiometer measurements. *J. Appl. Meteor.*, **38**, 633–664, doi:10.1175/1520-0450(1999)038<0633:ALHDIT>2.0.CO;2.

Oolman, L., and L. Leon, 2009: NSF/NCAR C-130 Wyoming Cloud Radar (WCR) data, 0905-0941Z, 02 November 2008. UCAR Earth Observing Laboratory, accessed 6 October 2014. [Available online at http://data.eol.ucar.edu/codiac/dss/id=89.148.]

Rapp, A. D., M. Lebsock, and T. L'Ecuyer, 2013: Low cloud precipitation climatology in the southeastern Pacific marine stratocumulus region using CloudSat. *Environ. Res. Lett.*, **8**, 014027, doi:10.1088/1748-9326/8/1/014027.

Reed, R. J., and E. E. Recker, 1971: Structure and properties of synoptic-scale wave disturbances in the equatorial western Pacific. *J. Atmos. Sci.*, **28**, 1117–1133, doi:10.1175/1520-0469(1971)028<1117:SAPOSS>2.0.CO;2.

Riehl, H., and J. S. Malkus, 1958: On the heat balance in the equatorial trough zone. *Geophysica*, **6**, 503–538.

Saleeby, S. M., and W. R. Cotton, 2004: A large-droplet mode and prognostic number concentration of cloud droplets in the Colorado State University Regional Atmospheric Modeling System (RAMS). Part I: Module descriptions and supercell test simulations. *J. Appl. Meteor.*, **43**, 182–195, doi:10.1175/1520-0450(2004)043<0182:ALMAPN>2.0.CO;2.

——, and S. C. van den Heever, 2013: Developments in the CSU-RAMS aerosol model: Emissions, nucleation, regeneration, deposition, and radiation. *J. Appl. Meteor. Climatol.*, **52**, 2601–2622, doi:10.1175/JAMC-D-12-0312.1.

——, S. R. Herbener, S. C. van den Heever, and T. S. L'Ecuyer, 2015: Impacts of cloud droplet nucleating aerosols on shallow tropical convection. *J. Atmos. Sci.*, **72**, 1369–1385, doi:10.1175/JAS-D-14-0153.1.

Schumacher, C., R. A. Houze, and I. Kraucunas, 2004: The tropical dynamical response to latent heating estimates derived from the TRMM Precipitation Radar. *J. Atmos. Sci.*, **61**, 1341–1358, doi:10.1175/1520-0469(2004)061<1341:TTDRTL>2.0.CO;2.

——, M. H. Zhang, and P. E. Ciesielski, 2007: Heating structures of the TRMM field campaigns. *J. Atmos. Sci.*, **64**, 2593–2610, doi:10.1175/JAS3938.1.

——, P. E. Ciesielski, and M. H. Zhang, 2008: Tropical cloud heating profiles: Analysis from KWAJEX. *Mon. Wea. Rev.*, **136**, 4289–4300, doi:10.1175/2008MWR2275.1.

Shannon, C., 1948: A mathematical theory of communication. *Bell Syst. Tech. J.*, **27**, 379–423, doi:10.1002/j.1538-7305.1948.tb01338.x.

Sheffield, A. M., S. M. Saleeby, and S. C. van den Heever, 2015: Aerosol-induced mechanisms for cumulus congestus growth. *J. Geophys. Res. Atmos.*, **120**, 8941–8952, doi:10.1002/2015JD023743.

Shige, S., Y. N. Takayabu, W.-K. Tao, and D. E. Johnson, 2004: Spectral retrieval of latent heating profiles from TRMM PR data. Part I: Development of a model-based algorithm. *J. Appl. Meteor.*, **43**, 1095–1113, doi:10.1175/1520-0450(2004)043<1095:SROLHP>2.0.CO;2.

——, ——, ——, and C.-L. Shie, 2007: Spectral retrieval of latent heating profiles from TRMM PR data. Part II: Algorithm improvement and heating estimates over tropical ocean regions. *J. Appl. Meteor. Climatol.*, **46**, 1098–1124, doi:10.1175/JAM2510.1.

——, ——, and ——, 2008: Spectral retrieval of latent heating profiles from TRMM PR data. Part III: Estimating apparent moisture sink profiles over tropical oceans. *J. Appl. Meteor. Climatol.*, **47**, 620–640, doi:10.1175/2007JAMC1738.1.

——, ——, S. Kida, W.-K. Tao, X. Zeng, C. Yokoyama, and T. L'Ecuyer, 2009: Spectral retrieval of latent heating profiles from TRMM PR data. Part IV: Comparisons of lookup tables from two- and three-dimensional cloud-resolving model simulations. *J. Climate*, **22**, 5577–5594, doi:10.1175/2009JCLI2919.1.

Simpson, J., R. F. Adler, and G. R. North, 1988: A proposed Tropical Rainfall Measuring Mission (TRMM) satellite. *Bull. Amer. Meteor. Soc.*, **69**, 278–295, doi:10.1175/1520-0477(1988)069<0278:APTRMM>2.0.CO;2.

Stephens, G. L., and Coauthors, 2008: CloudSat mission: Performance and early science after the first year of operation. *J. Geophys. Res.*, **113**, D00A18, doi:10.1029/2008JD009982.

Tanelli, S., S. L. Durden, E. Im, K. S. Pak, D. G. Reinke, P. Partain, J. M. Haynes, and R. T. Marchand, 2008: CloudSat's Cloud Profiling Radar after two years in orbit: Performance, calibration, and processing. *IEEE Trans. Geosci. Remote Sens.*, **46**, 3560–3573, doi:10.1109/TGRS.2008.2002030.

Tao, W.-K., S. Lang, J. Simpson, and R. Adler, 1993: Retrieval algorithms for estimating the vertical profiles of latent heat release: Their applications for TRMM. *J. Meteor. Soc. Japan*, **71**, 685–700.

——, ——, X. Zeng, S. Shige, and Y. Takayabu, 2010: Relating convective and stratiform rain to latent heating. *J. Climate*, **23**, 1874–1893, doi:10.1175/2009JCLI3278.1.

——, and Coauthors, 2016: TRMM latent heating retrieval: Applications and comparisons with field campaigns and large-scale analyses. *Multiscale Convection-Coupled Systems in the Tropics: A Tribute to the Late Professor Yanai*, *Meteor. Monogr.*, No. 56, Amer. Meteor. Soc., 2.1–2.34, doi:10.1175/AMSMONOGRAPHS-D-15-0013.1.

Thompson, R. M., S. W. Payne, E. E. Recker, and R. J. Reed, 1979: Structure and properties of synoptic-scale wave disturbances in the Intertropical Convergence Zone of the eastern Atlantic. *J. Atmos. Sci.*, **36**, 53–72, doi:10.1175/1520-0469(1979)036<0053:SAPOSS>2.0.CO;2.

Walko, R. L., and Coauthors, 2000: Coupled atmosphere–biophysics–hydrology models for environmental modeling. *J. Appl.*

Meteor., **39**, 931–944, doi:10.1175/1520-0450(2000)039<0931:CABHMF>2.0.CO;2.

Wood, N. B., T. S. L'Ecuyer, A. J. Heymsfield, G. L. Stephens, D. R. Hudak, and P. Rodriguez, 2014: Estimating snow microphysical properties using collocated multisensor observations. *J. Geophys. Res. Atmos.*, **119**, 8941–8961 doi:10.1002/2013JD021303.

Yanai, M., S. Esbensen, and J.-H. Chu, 1973: Determination of bulk properties of tropical cloud clusters from large-scale heat and moisture budgets. *J. Atmos. Sci.*, **30**, 611–627, doi:10.1175/1520-0469(1973)030<0611:DOBPOT>2.0.CO;2.

Yang, S., and E. A. Smith, 1999: Moisture budget analysis of TOGA COARE area using SSM/I-retrieved latent heating and large-scale Q2 estimates. *J. Atmos. Oceanic Technol.*, **16**, 633–655, doi:10.1175/1520-0426(1999)016<0633:MBAOTC>2.0.CO;2.

Zhang, C., and Coauthors, 2010: MJO signals in latent heating: Results from TRMM retrievals. *J. Atmos. Sci.*, **67**, 3488–3508, doi:10.1175/2010JAS3398.1.